ce/papers
The online collection for conference papers in civil engineering
Ernst & Sohn A Wiley Brand

Check for updates

ORIGINAL ARTICLE

SDSS 2022
The International Colloquium on Stability and Ductility of Steel Structures
14-16 September, University of Aveiro, Portugal
Ernst & Sohn A Wiley Brand

# Microstructure, Mechanical Properties and Cross-sectional Behaviour of Additively Manufactured Stainless Steel Cylindrical Shells

Ruizhi Zhang[1], Mohsen Amraei, Heidi Piili, Leroy Gardner

**Correspondence**

Dr. Ruizhi Zhang
Imperial College London
Skempton Building
Imperial College Road
South Kensington
London
SW7 2BU
Email: r.zhang18@imperial.ac.uk

**Abstract**

Powder bed fusion (PBF) is an additive manufacturing method that enables complex metallic components to be manufactured with high precision. The microstructure, mechanical properties and cross-sectional behaviour of PBF additively manufactured stainless steel circular hollow sections are investigated through experiments in this paper, with a view to applications in construction. The experimental programme included tensile coupon tests, microstructural characterisation, initial geometric imperfection measurements and compression tests on PBF 316L stainless steel cylindrical shells with large diameter-to-thickness ($D/t$) ratios. Advanced measurement methods – 3D laser scanning and digital image correlation, were employed to measure the specimen geometries prior to testing and deformation fields during testing, respectively. The possible anisotropy in mechanical properties was examined through tensile coupon tests and correlated with the underlying microstructural and textural features. Compression tests were performed to investigate the resistance against local buckling of thin-walled cylindrical shells produced by PBF. All cylindrical shells buckled below their yield loads with a chequerboard failure mode and revealed the anticipated trend of reducing capacity relative to the yield load with increasing local slenderness, reflecting the increasing susceptibility to local buckling.

**Keywords**

Additive manufacturing, Cylindrical shells, Digital image correlation (DIC), Microstructure, Laser scanning, Powder bed fusion (PBF), Stainless steel, Compression tests, Tensile coupon tests, 3D printing

## 1 Introduction

Additive manufacturing (or 3D printing) has gained considerable attention due to its ability to manufacture complex structural components with high precision. An important challenge to be overcome before additively manufactured structural elements can be used more widely in the construction industry is the development of structural design guidance, supported by a suitable pool of experimental data. Thick-walled additively manufactured (AM) circular hollow sections have been considered in previous studies [1]. Thin-walled circular cylindrical shells, additively manufactured by powder bed fusion (PBF), are examined experimentally in the present paper from a microstructural, material and cross-sectional perspective.

The experimental investigation included tensile coupon tests, optical microscopy (OM) and scanning electron microscopy (SEM) observations and texture analysis on PBF 316L stainless steel, initial geometric imperfection measurements and five axial compression tests on stainless steel cylindrical shells with different slendernesses. All the specimens were printed in the Laboratory of Laser Processing of the School of Energy Systems at LUT University. The OM analysis was performed in the Engineering Alloys Lab, while the SEM and electron backscatter diffraction (EBSD) analyses were conducted in the Harvey Flower Electron Microscopy Suite, both in the Department of Materials at Imperial College London. The tensile coupon tests and cross-section compression tests were conducted in the Structures Laboratory of the Department of Civil and Environmental Engineering at Imperial College London.

1. Imperial College London, London, UK.

This is an open access article under the terms of the Creative Commons Attribution License, which permits use, distribution and reproduction in any medium, provided the original work is properly cited.

© 2022 The Authors. Published by Ernst & Sohn GmbH. 

## 2 Specimen manufacture

The adopted feedstock material was austenitic grade 316L stainless steel powder [2]. All the test coupons and shells were manufactured at a deposition rate of 13.3 $cm^3$/hour through laser-based powder bed fusion using a modified EOSINT M-series PBF research machine that can print components with a maximum size of approximately 400 mm×400 mm×400 mm. The PBF manufacturing process features a high-energy laser beam scanning across a layer of metallic powder, melting the powder at programmed locations according to an input STL model; a more detailed description of this process is provided in [1]. The coupons and shells were printed vertically, with their longitudinal axis perpendicular to the print layers (i.e. $\vartheta$=90°, where $\vartheta$ is the angle between the longitudinal axis of the specimen and the build plate). A photograph of shell specimens within the same batch during printing is shown in Figure 1, while Figure 2 shows all the completed cylindrical shell specimens.

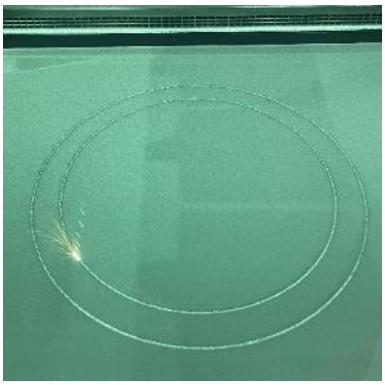


**Figure 1** Shell specimens during printing



**Figure 2** All completed PBF shell specimens (with decreasing slenderness from left to right)

## 3 Tensile coupon tests

Six vertical 316L tensile coupons, with dog-bone shapes, were tested using a 250 kN Instron 8802 testing machine, as shown in Figure 3. Prior to tensile testing, a series of standard gauge lengths ($5.65\sqrt{S_0}$, where $S_0$ is the original cross-sectional area of the parallel length) were marked onto the front and back faces for the post-test measurement of the fracture strains. A four-camera LaVision DIC system [3] was employed to measure strains over the parallel length on both coupon faces, with two cameras observing each side. The front and back faces of the coupons were painted white and sprayed with a random black speckle pattern to create trackable features along the parallel length. The testing machine was operated under displacement control, with two strain rates of 0.007% $s^{-1}$ and 0.025% $s^{-1}$ before and after yielding and a gradual transition between the two rates to avoid any abrupt change in rate, as recommended in EN ISO 6892-1 [4]. The applied load was measured using a load cell within the testing machine and recorded via an analogue to digital converter within the DIC system. The frequency for capturing the loading data and DIC images, was set to 1 Hz. The longitudinal strain was obtained by averaging the strains over the parallel length on both coupon faces.

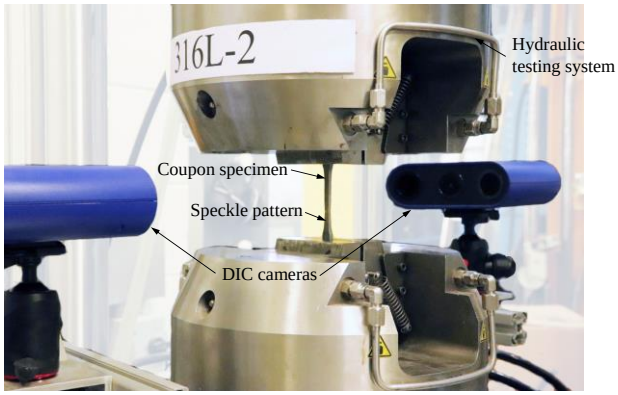



**Figure 3** Tensile coupon test setup with 3D stereo-DIC system

The measured engineering tensile stress-strain curves obtained from the coupon tests on the 316L stainless steel are plotted in Figure 4, and the key material properties – the Young's modulus $E$, 0.2% proof strength $\sigma_{0.2}$, 1.0% proof strength $\sigma_{1.0}$, ultimate tensile strength $\sigma_u$, strain at the ultimate tensile strength $\varepsilon_u$ and fracture strain over the marked gauge length $\varepsilon_f$, are reported in Table 1. Also presented are the Ramberg-Osgood parameter $n$ [5] and the extended strain hardening parameters $m_{1.0}$ and $m_u$ [6–8], which were fitted to the measured stress-strain curves using the method described in [9,10].

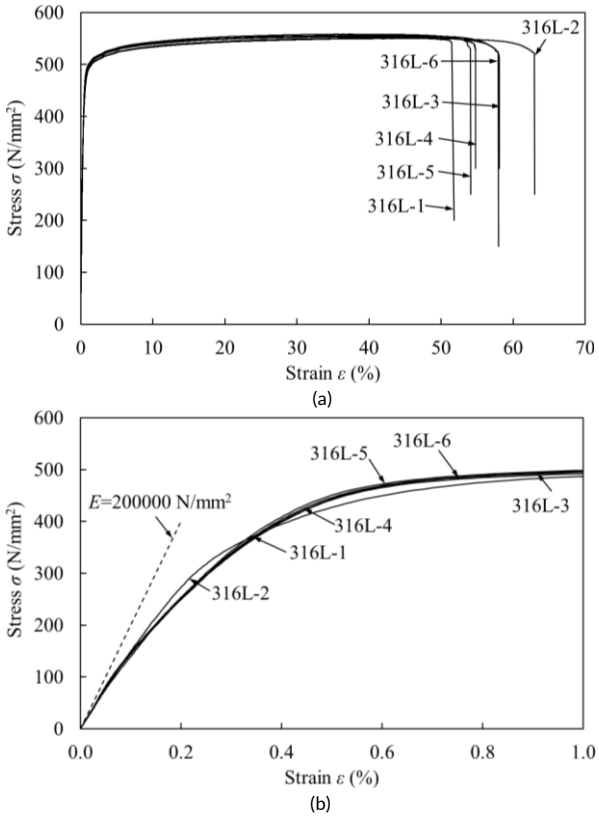



**Figure 4** Stress-strain curves obtained from PBF 316L stainless steel tensile coupons over the (a) full range and (b) initial range

**Table 1** Measured material properties from vertical tensile coupon tests

| Coupon | $E$ (N/mm²) | $\sigma_{0.2}$ (N/mm²) | $\sigma_{1.0}$ (N/mm²) | $\sigma_u$ (N/mm²) | $\varepsilon_u$ (%) | $\varepsilon_f$ (%) | $n$ | $m_{1.0}$ | $m_u$ |
|---|---|---|---|---|---|---|---|---|---|
| 316L-1 | 174100 | 439 | 499 | 551 | 39.6 | 60.7 | 3.4 | 6.0 | 7.4 |
| 316L-2 | 162100 | 420 | 496 | 550 | 45.7 | 62.0 | 5.1 | 7.6 | 9.4 |
| 316L-3 | 170900 | 433 | 502 | 556 | 39.7 | 59.3 | 3.0 | 6.6 | 8.1 |
| 316L-4 | 164400 | 437 | 503 | 555 | 36.7 | 59.0 | 3.0 | 6.4 | 7.9 |
| 316L-5 | 172500 | 443 | 505 | 558 | 35.6 | 58.5 | 3.0 | 5.9 | 7.2 |
| 316L-6 | 160000 | 439 | 502 | 553 | 37.4 | 60.5 | 3.3 | 6.2 | 7.8 |
| Average | 167300 | 435 | 501 | 554 | 39.1 | 60.0 | 3.5 | 6.5 | 8.0 |

25097075, 2022, 4, Downloaded from https://onlinelibrary.wiley.com/doi/10.1002/cepa.1792 by Imperial College London, Wiley Online Library on [02/04/2025]. See the Terms and Conditions (https://onlinelibrary.wiley.com/terms-and-conditions) on Wiley Online Library for rules of use; OA articles are governed by the applicable Creative Commons License

The measured 0.2% proof stress, ultimate stress and fracture strain of the PBF 316L stainless steel were comparable to those provided in the EOS material datasheet [2]. Generally, the PBF 316L base metal had higher proof and ultimate strengths ($\sigma_{0.2}$, $\sigma_{1.0}$ and $\sigma_u$) than conventionally formed 316L stainless steel [11–13]. The increase in ultimate strength $\sigma_u$ is smaller than that of the 0.2% proof stress $\sigma_{0.2}$, and the fracture strain $\varepsilon_f$ of the PBF base metal and the conventionally formed material is similar. The measured Young's moduli $E$ of the PBF 316L stainless steel coupons were slightly lower than the typically assumed value of $E$=200000 N/mm$^2$ for conventional stainless steels [9].

## 4 Microstructure characterisation

After the destructive tensile coupon tests, small metallurgical samples were sectioned from the gripped regions of the 316L-4 coupon. To investigate the potential anisotropic mechanical properties resulting from the laser scan paths, three faces of the PBF samples, parallel to three orthogonal planes TD2-BD, TD1-TD2 and TD1-BD (see Figure 5), were examined. All samples were prepared for microstructural characterisation in accordance with ASTM E3-11 [14]. The samples were ground, polished to a mirror finish and then electrolytically etched using a 10%wt oxalic acid solution at 6 volts for 60 seconds as recommended by ASTM E407-07 [15]. The as-etched surfaces were first examined using an Olympus BX51 optical microscope. The metallographic samples for EBSD characterisation were tilted to 70° relative to the horizontal, positioned at a working distance of 15 mm and scanned at a beam acceleration voltage of 20 kV using an FEI Quanta 650 SEM equipped with a Bruker eFlash$^{HD}$ EBSD detector and Argus forescatter diodes (FSD) imaging. EBSD patterns were acquired using the Esprit 2.2 software [16] and reconstructed using the Matlab toolbox MTEX 5.6.0 [17].

Figure 5 shows 3D-view optical micrographs of the examined PBF 316L stainless steel. The samples exhibited a typical layered microstructure, characterised by melt pool boundaries generated along the laser scanning paths and a chequerboard macrostructure in the scan layers.

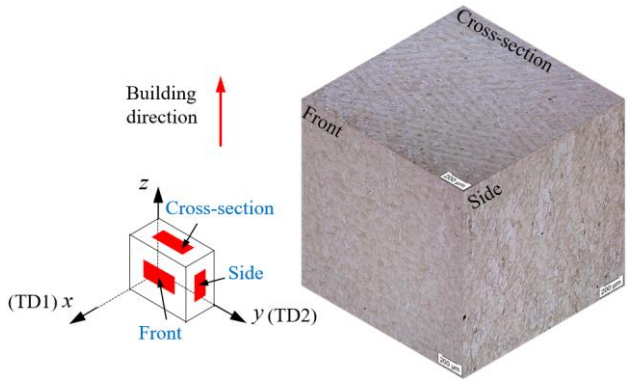



**Figure 5** 3D OM microstructure reconstruction of samples extracted from PBF coupon 316L-4, showing the laser tracks along the build direction and the scanning pattern

Inspection of the SEM images reveals cellular solidification microstructure within the melt pools, as shown in Figure 6(a). Periodic melt pools were revealed at high magnification, showing a half ellipse morphology and a depth and width of about 70 µm and 130 µm, respectively. Note that the differently oriented melt pools are the result of the bidirectional scanning strategy, i.e. 45° rotation after each layer, and partial remelting occurred in the overlapping melt pools. A continuous epitaxial growth roughly along the build direction, which follows the direction of the maximum temperature gradient, results in the occurrence of slender columnar grains near the centreline of the melt pools.

The examined PBF 316L stainless steel was found to comprise a single-phase austenitic face-centred cubic (FCC) crystal structure through EBSD analysis. Figure 6 presents the EBSD orientation maps with respect to the build direction (IPF-BD) of the front sample, coupled with the (100), (110) and (111) pole figures. Wide/long columnar grains grew mainly along the <001> and <011> directions, which are the preferred growth directions for FCC crystals [18,19]. Side-branching of crystals between adjacent deposition tracks is prevalent due to the frequent changes in heat flux across the melt pool boundaries, which leads to the strongest texture in these locations with the maximum intensity of 4.0 times the random intensity, as shown in the (111) pole figure in Figure 6(c). The average measured grain size was 36.7 µm in the scanned areas of the front sample, which was finer than their conventionally produced counterparts, leading to a higher measured strength, following the Hall-Petch relationship [20,21]. The examined 316L stainless steel exhibited a weak texture, which resulted in slight anisotropy in the Young's modulus.

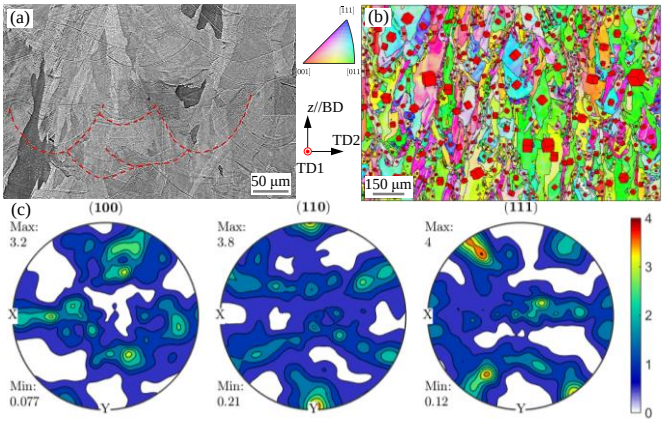



**Figure 6** (a) SEM micrograph, (b) EBSD IPF-BD orientation map with respect to the build direction and (c) pole figures of the front sample extracted from the 316L-4 coupon

## 5 Geometric measurements

The shell test specimens had nominal cross-section sizes (outer diameter $D$ × thickness $t$) of C150×1.0, C180×1.0, C150×0.7, C180×0.7 and C200×0.7, resulting in a range of different cross-section slendernesses. The geometric properties of the shell test specimens were determined before end potting through (i) hand measurements using digital callipers, (ii) Archimedes' method, and (iii) 3D laser-scanning, with the setup shown in Figure 7. The average outer diameter $D$, wall thickness $t$ (at both ends) and length $L$ were measured at 30° intervals around the circumference of the specimens using callipers. The cross-sectional area $A$ was determined as the measured volume using Archimedes' method $V_{Arch}$ divided by the length measured using callipers $L$.

Local imperfection measurements were made based on the geometries captured using 3D laser-scanning. The outer and inner surfaces of the shell specimens were scanned using a Faro ScanARM laser scanner and pre-processed in Geomagic Wrap [22]. The pre-processed 3D point data were saved as a polygon model and imported in Rhino 3D [23]; the model was then aligned with the global coordinate system and contoured into cross-section slices along the specimen length. A series of vertical planes were defined through the cross-section slices to provide sets of longitudinal points along the lengths of the shells. A straight line was fitted to each set of longitudinal points using linear regression, which served as a reference datum from which the deviations were determined, representing the local imperfections [1,24]. The measured imperfection distribution for specimen C200×0.7 is shown in Figure

25097075, 2022, 4, Downloaded from https://onlinelibrary.wiley.com/doi/10.1002/cepa.1792 by Imperial College London, Wiley Online Library on [02/04/2025]. See the Terms and Conditions (https://onlinelibrary.wiley.com/terms-and-conditions) on Wiley Online Library for rules of use; OA articles are governed by the applicable Creative Commons License

8, where outward deviations are recorded as positive, and inward deviations are recorded as negative. The maximum deviation over the entire specimen was taken as the local imperfection amplitude $\omega_{max}$, which lay between 0.24 mm and 0.37 mm (corresponding to 0.2$t$~0.5$t$) for all specimens, as reported in Table 2.

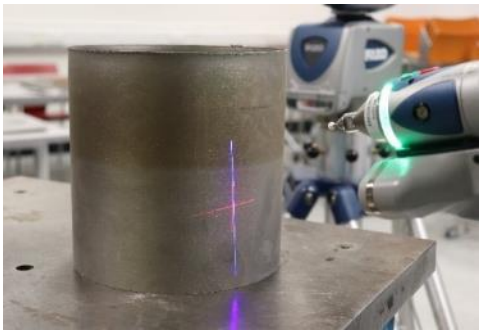


**Figure 7** Setup for geometric measurements using 3D laser-scanning

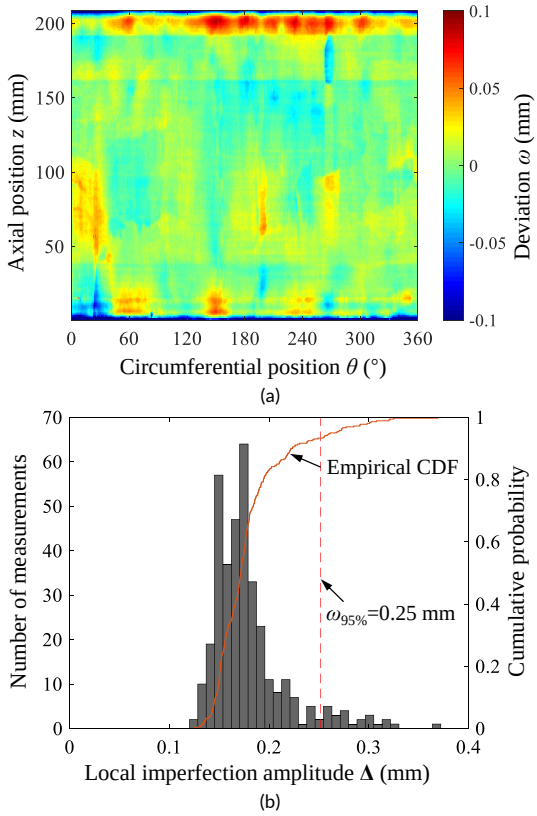



**Figure 8** (a) Measured imperfection distribution and (b) histogram and CDFs of longitudinal imperfections in shell specimen C200×0.7

A probabilistic study was also carried out to examine the variation in longitudinal imperfection amplitudes around the circumference of the shell specimens. Histograms of local imperfection amplitudes from 360 measurements (at intervals of 1°) were constructed, and are shown for a typical cylindrical shell (specimen C200×0.7) in Figure 8(b), along with the empirical cumulative distribution function (CDF) curves for the 360 measurements. A CDF value represents the probability that a randomly selected imperfection amplitude $\Delta$ will be less than a given imperfection amplitude value $\omega_p$, i.e. $P(\Delta<\omega_p)$ [25,26]. The $P(\Delta<\omega_p)$=95% characteristic imperfection value $\omega_{95\%}$ represents an imperfection amplitude that would not be expected to be exceeded in 95% of PBF shell specimens. All dimensions and characteristic imperfection values for the shell test specimens are summarised in Table 2. The measured imperfection amplitudes ($\omega_{max}$ and $\omega_{95\%}$) were approximately equal to $0.02(Dt)^{1/2}$, where $D$ and $t$ are the measured outer diameter and wall thickness of the shell specimens.

**Table 2** Measured geometric properties of PBF cylindrical shell specimens

| Specimen | $D$ (mm) | $t$ (mm) | $L$ (mm) | $V_{Arch}$ (mm$^3$) | $A$ (mm$^2$) | $\omega_{max}$ (mm) | $\omega_{95\%}$ (mm) |
|---|---|---|---|---|---|---|---|
| **C150×1.0** | 149.9 | 1.13 | 159.6 | 76520 | 479.3 | 0.32 | 0.28 |
| **C180×1.0** | 149.7 | 0.82 | 159.8 | 109458 | 576.8 | 0.27 | 0.27 |
| **C150×0.7** | 180.2 | 1.16 | 189.8 | 55209 | 345.4 | 0.24 | 0.21 |
| **C180×0.7** | 179.8 | 0.80 | 189.8 | 78114 | 411.7 | 0.27 | 0.25 |
| **C200×0.7** | 199.5 | 0.77 | 209.0 | 96349 | 461.1 | 0.37 | 0.25 |

## 6 Compression tests

A total of five axial compression tests were carried out to investigate the compressive response and load-bearing capacity of the cylindrical shells manufactured by PBF. For each shell specimen, the printed (top) end had a high degree of manufacturing precision, while the lower end that was cut from the build plate had to be machined flat and square, removing any residual support structures, to facilitate the uniform introduction of load during testing. Wooden blocks were precisely machined and inserted into the specimens to strengthen the clamped regions during end machining. Prior to testing, the top and bottom ends of each specimen were confined using Araldite 2011 epoxy adhesive potting, supported by outer and inner metallic ring stiffeners with a thickness of 10 mm, in order to avoid premature end failure.

All the tests were conducted using an Instron 3500 kN-SPL testing machine; the test setup is presented in Figure 9. A ball seating was placed between the crosshead of the testing machine and the top end platen to accommodate any potential gaps and to ensure that the axial loads were uniformly applied to the cylinder edges. Hardened end plates were placed at both ends of the specimens to prevent damage to the testing machine from the high localised stresses. Prior to testing, the surface of each specimen was painted white and sprayed with a random black speckle pattern with a minimum size of 3 to 5 pixels to create trackable features. A four-camera LaVision DIC system was adopted to track the relative movement of the speckles from two sides at 90° to each other, with two cameras monitoring each side. The axial deformations were measured using three potentiometers and three strain gauges affixed to the mid-height of each specimen at 120° intervals, as shown in Figure 9. The compressive load was applied under displacement control such that a compressive strain rate of 0.1% min$^{-1}$ was achieved, and recorded using a load cell within the testing machine. The test outputs, including the axial load, top platen movement, potentiometer and strain gauge readings and DIC images were recorded at a frequency of 1 Hz.

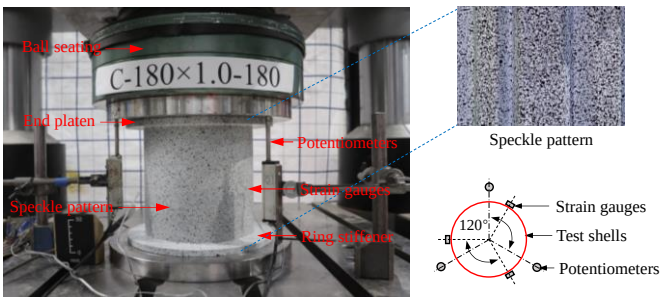



**Figure 9** Experimental configuration for shell compression tests

The post-ultimate distributions of out-of-plane deformations of all test specimens are presented in Figure 10 for better visualisation of the failure modes, where positive deformations (coloured in red) are outward, while the negative deformations (coloured in purple) are inward. The test cylindrical shells failed by 'chequerboard' local buckling with one half longitudinal wave and 5 to 9 circumferential waves, where the number of circumferential waves $m$ for each shell

25097075, 2022, 4, Downloaded from https://onlinelibrary.wiley.com/doi/10.1002/cepa.1792 by Imperial College London, Wiley Online Library on [02/04/2025]. See the Terms and Conditions (https://onlinelibrary.wiley.com/terms-and-conditions) on Wiley Online Library for rules of use; OA articles are governed by the applicable Creative Commons License

is reported in Table 3.

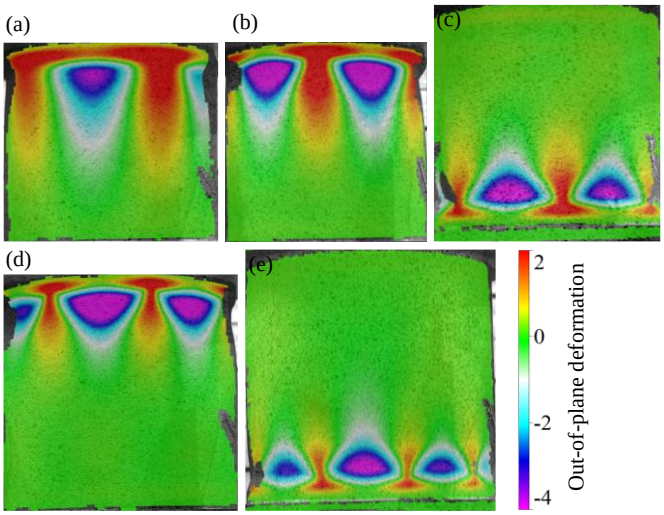



**Figure 10** Post-ultimate out-of-plane deformations (unit: mm) of cylindrical shells, with increasing slenderness from top left to bottom right

A typical axial load-end shortening curve and DIC results from the compression tests are presented in Figure 11, where the evolution of the axial strain fields can be clearly seen. All axial load-end shortening curves obtained from (i) the potentiometer and strain gauge readings (LVDT+SG in Figure 12), with the elastic deformations of the end platens eliminated [27], and (ii) the DIC data, are plotted in Figure 12. The two approaches to the calculation of end shortening are shown to produce essentially identical results. All cylindrical shells failed at a load level below the yield load $\sigma_{0.2}A$, and there was a reduced capacity relative to the yield load with increasing local slenderness, reflecting the increasing vulnerability to local buckling. The buckling of specimen C200×0.7 occurred abruptly, with a sudden drop in the applied load; the shell stablished again at about half of the peak load. The key test outputs, including the number of circumferential waves $m$, the peak load $N_u$, the end shortening at the peak load $\delta_u$ and the ratio between the peak load $N_u$ and the yield load $N_y$, are reported in Table 3, along with the local slenderness values and corresponding cross-section class, as defined in EN 1993-1-4 [28], and the local cross-section slenderness $\bar{\lambda}_c$ [1].

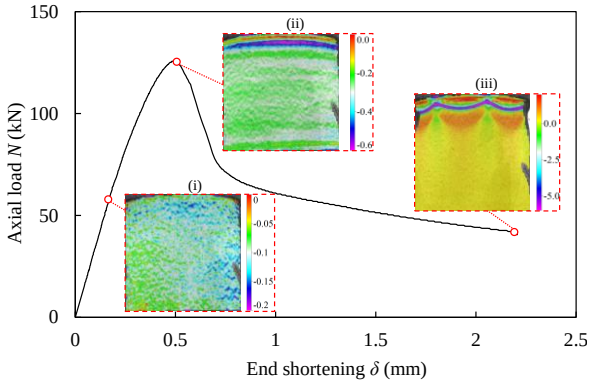



**Figure 11** Typical axial load end-shortening curve and DIC results from compression tests on specimen C180×0.7, showing axial strain distributions (unit: %) (i) at $0.5N_u$, (ii) just after $N_u$ and (iii) when unloading

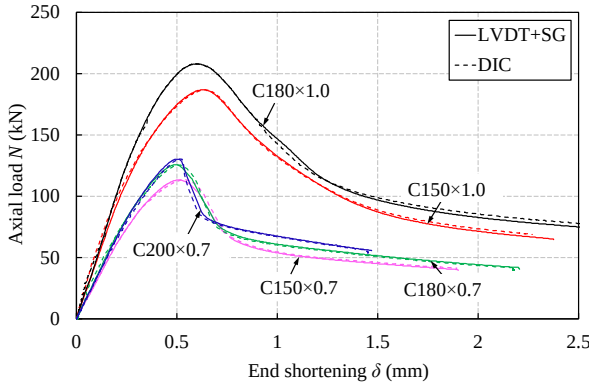



**Figure 12** Measured axial load end-shortening curves of all test specimens

**Table 3** Geometric properties and key test results of shells

| Specimen | $D/t\epsilon^2$ | EC3 class | $\bar{\lambda}_c$ | $m$ | $N_u$ (kN) | $\delta_u$ (mm) | $N_u/N_y$ |
|---|---|---|---|---|---|---|---|
| **C150×1.0** | 307.7 | 4 | 0.53 | 5 | 186.8 | 0.62 | 0.90 |
| **C180×1.0** | 362.2 | 4 | 0.58 | 6 | 208.2 | 0.59 | 0.83 |
| **C150×0.7** | 422.6 | 4 | 0.63 | 7 | 113.3 | 0.50 | 0.75 |
| **C180×0.7** | 521.6 | 4 | 0.69 | 8 | 125.7 | 0.49 | 0.70 |
| **C200×0.7** | 600.0 | 4 | 0.74 | 9 | 130.2 | 0.49 | 0.65 |

## 7 Conclusions

This paper presents an experimental study into the cross-sectional behaviour of additively manufactured circular cylindrical shells subjected to axial compression. Five cylindrical shells with a range of local slendernesses were additively manufactured by powder bed fusion (PBF) using 316L stainless steel powder. The experiments represent a significant expansion to the very limited existing dataset on PBF stainless steel cylindrical shells, and were accompanied by mechanical and microstructural testing of the material. 3D laser-scanning and digital image correlation (DIC) techniques were employed to capture the geometries and deformation fields of the test specimens, respectively. The test setup, test procedure, full load end-shortening curves, failure modes and key test results of the compression tests have been fully reported. All cylindrical shells buckled in a chequerboard pattern and revealed the anticipated trend of reducing capacity relative to the yield load with increasing local slenderness, reflecting the greater vulnerability to local buckling.

## 8 Acknowledgements

The authors would like to acknowledge the contribution of the LUT Laser Laboratory for building the test specimens and Les Clark and Gordon Herbert for their assistance in the Structures Laboratory at Imperial College London. The financial support from the China Scholarship Council is also gratefully acknowledged.

## References

[1] Zhang R.; Gardner L.; Buchanan C.; Matilainen VP.; Piili H.; Salminen A. (2021). *Testing and analysis of additively manufactured stainless steel CHS in compression*. Thin-Walled Structures **159**, S.107270.

[2] EOS (2017). *EOS StainlessSteel 316L*.

[3] LaVision (2017). *DaVis 8*.

[4] CEN (2016). *Metallic materials — Tensile testing*. Metallic Materials — Tensile Testing Part 1: Method of Test at Room Temperature.

25097075, 2022, 4, Downloaded from https://onlinelibrary.wiley.com/doi/10.1002/cepa.1792 by Imperial College London, Wiley Online Library on [02/04/2025]. See the Terms and Conditions (https://onlinelibrary.wiley.com/terms-and-conditions) on Wiley Online Library for rules of use; OA articles are governed by the applicable Creative Commons License

[5] Ramberg W.; Osgood WR. (1943). Description of stress-strain curves by three parameters. Washington, D.C.

[6] Rasmussen KJR. (2003). *Full-range stress–strain curves for stainless steel alloys*. Journal of Constructional Steel Research **59**, S.47–61.

[7] Gardner L.; Ashraf M. (2006). *Structural design for non-linear metallic materials*. Engineering Structures **28**, S.926–934.

[8] Mirambell E.; Real E. (2000). *On the calculation of deflections in structural stainless steel beams: An experimental and numerical investigation*. Journal of Constructional Steel Research **54**, S.109–133.

[9] Arrayago I.; Real E.; Gardner L. (2015). *Description of stress–strain curves for stainless steel alloys*. Materials & Design **87**, S.540–552.

[10] Gardner L.; Yun X. (2018). *Description of stress-strain curves for cold-formed steels*. Construction and Building Materials **189**, S.527–538.

[11] Mower TM.; Long MJ. (2016). *Mechanical behavior of additive manufactured, powder-bed laser-fused materials*. Materials Science and Engineering A **651**, S.198–213.

[12] Yadollahi A.; Shamsaei N.; Thompson SM.; Seely DW. (2015). *Effects of process time interval and heat treatment on the mechanical and microstructural properties of direct laser deposited 316L stainless steel*. Materials Science and Engineering: A **644**, S.171–183.

[13] ASTM (2019). *Standard Specification for Stainless Steel Forgings*. ASTM A473-15.

[14] ASTM (2012). *Standard Guide for Preparation of Metallographic Specimens Standard Guide for Preparation of Metallographic Specimens 1*. ASTM International.

[15] ASTM (2015). *Standard Practice for Microetching Metals and Alloys ASTM E407-07:2015*.

[16] Bruker (2018). *Quantax Esprit 2.2*.

[17] Bachmann, F., Hielscher, R. and Schaeben H. (2010). Texture analysis with MTEX–free and open source software toolbox. Solid State Phenomena, Trans Tech Publications Ltd.

[18] Pham MS.; Dovgyy B.; Hooper PA.; Gourlay CM.; Piglione A. (2020). *The role of side-branching in microstructure development in laser powder-bed fusion*. Nature Communications **11**, S.1–12.

[19] Bahshwan M.; Myant CW.; Reddyhoff T.; Pham MS. (2020). *The role of microstructure on wear mechanisms and anisotropy of additively manufactured 316L stainless steel in dry sliding*. Materials and Design **196**, S.109076.

[20] Hall EO. (1951). *The deformation and ageing of mild steel: III Discussion of results*. Proceedings of the Physical Society Section B **64**, S.747–753.

[21] Petch NJ. (1953).*The Cleavage Strength of Polycrystals*. Journal of the Iron and Steel Institute **174**, S.25–28.

[22] 3D Systems (2017). *Geomagic Wrap*.

[23] Rhino 3D (2012). *Rhinoceros 5.0*.

[24] Meng X.; Gardner L. (2020).*Testing of hot-finished high strength steel SHS and RHS under combined compression and bending*. Thin-Walled Structures **148**, S.106262.

[25] Schafer BW.; Peköz T. (1998). *Computational modeling of cold-formed steel: characterizing geometric imperfections and residual stresses*. Journal of Constructional Steel Research **47**, S.193–210.

[26] Schafer BW. (1996). *A Probabilistic Examination of the Ultimate Strength of Cold- formed Steel Elements*.

[27] Centre for Advanced Structural Engineering (1990). Compression tests of stainless steel tubular columns. Sydney.

[28] CEN (2015). *Eurocode 3-Design of steel structures. Part 1-4: General rules-Supplementary rules for stainless steels*. Design of Structural Elements.

25097075, 2022, 4, Downloaded from https://onlinelibrary.wiley.com/doi/10.1002/cepa.1792 by Imperial College London, Wiley Online Library on [02/04/2025]. See the Terms and Conditions (https://onlinelibrary.wiley.com/terms-and-conditions) on Wiley Online Library for rules of use; OA articles are governed by the applicable Creative Commons License